Variability and Dynamics of the Yucatan Upwelling: High-Resolution Simulations

J. Jouanno, E. Pallàs-Sanz, J. Sheinbaum

AGU PUBLICATIONS

JGR

Journal of Geophysical Research: Oceans

RESEARCH ARTICLE

10.1002/2017JC013535

Variability and Dynamics of the Yucatan Upwelling: High-Resolution Simulations

J. Jouanno[1], E. Pallàs-Sanz[2], and J. Sheinbaum[2]

[1]LEGOS, IRD, Univ. Paul Sabatier, Observatoire Midi-Pyrénées, Toulouse, France, [2]Departamento de Oceanografía Física, CICESE, Ensenada, Baja California, Mexico

Key Points:
- Results show that the Yucatan upwelling is controlled by the interactions between the Loop Current and the Yucatan shelf
- High-frequency winds over the gulf lead to high-frequency fluctuations of the upwelling with a net contribution to the upwelling
- Key role played by a notch along the Yucatan shelf break in bringing cool waters to the shelf

Correspondence to:
J. Jouanno,
julien.jouanno@ird.fr

Citation:
Jouanno, J., Pallàs-Sanz, E., & Sheinbaum, J. (2018). Variability and dynamics of the Yucatan upwelling: High-resolution simulations. *Journal of Geophysical Research: Oceans*, *123*, 1251–1262. https://doi.org/10.1002/2017JC013535

Received 6 OCT 2017
Accepted 15 JAN 2018
Accepted article online 25 JAN 2018
Published online 15 FEB 2018

Abstract The Yucatan shelf in the southern Gulf of Mexico is under the influence of an upwelling that uplifts cool and nutrient rich waters over the continental shelf. The analysis of a set of high-resolution ($\Delta x = \Delta y \approx 2.8$ km) simulations of the Gulf of Mexico shows two dominant modes of variability of the Yucatan upwelling system: (1) a low-frequency mode related to variations in position and intensity of the Loop Current along the shelf, with upwelling intensified when the Loop Current is strong and approaches to the Yucatan shelf break and (2) a high-frequency mode with peak frequency in the 6–10 days band related to wind-forced coastal waves that force vertical velocities along the eastern Yucatan shelf break. To first order, the strength and position of the Loop Current are found to control the intensity of the upwelling, but we show that high-frequency winds also contribute (∼17%) to a net input of cool waters (<22.5°C) on the Yucatan shelf. Finally, although more observational studies are needed to corroborate the topographic character of the Yucatan upwelling system, this study reveals the key role played by a notch along the Yucatan shelf break: a sensitivity simulation without the notch shows a 55% reduction of the upwelling.

1. Introduction

The existence of an upwelling signal along the eastern Yucatan slope (see maps in Figure 1) was reported since the sixties by U.S. (e.g., Cochrane, 1966) and Soviet-Cuban expeditions (e.g., Belousov et al., 1966), but it is only thirty years later that the first detailed description of the Yucatan upwelling was published by Merino (1997). Based on hydrographic data gathered during four cruises, Merino (1997) shows that subsurface Caribbean waters, characterized by temperatures between 16 and 20°C and salinities between 36.1 and 36.5 psu upwell from 220 to 250 m depth and intrude over the Yucatan shelf. The observations indicate that the waters mainly enter at the notch located on the eastern Yucatan shelf-slope (between 22°N and 23°N; Figure 1b), and then move westward across the shelf. As highlighted in Merino (1997), the upwelled waters generally do not reach the surface, leading to the formation of a highly stratified two-layer water column over the shelf (see also Enriquez et al., 2013).

Coastal (near-shore) upwelling on the Yucatan shelf is, however, still visible in satellite data: the mean sea surface temperature (SST) observed in the Yucatan region shows the presence of surface waters on the Yucatan shelf that are cooler than the surrounding waters (Figure 2a), with the area covered by these cool waters nearly bounded by the 30 m isobath. Since upwelled waters over the shelf do not generally reach the ocean surface, the real magnitude of the upwelling is hidden from surface observations and limits the use of satellite data to study its variability, as commonly done for other upwelling systems.

The westward orientation of the mean wind stress is favorable to upwelling along the northern coast of the Yucatan peninsula (Figure 2c), but the coastal divergence of the surface waters has never been considered to be the leading mechanism controlling the eastern shelf Yucatan upwelling. Instead, results obtained from early and recent studies indicate that the upwelling would be of topographic nature and may result from the interaction between the intense western boundary current (Figure 2b) and the Yucatan shelf break (Cochrane, 1966; Enriquez & Mariño-Tapia, 2014; Merino, 1997) Nevertheless, Merino (1997) does not discard that the local wind may play an indirect role on the upwelling by inducing high-frequency variations in the Yucatan Current strength. At the northeast corner of Yucatan peninsula, Reyes-Mendoza et al. (2016) observed upwelling pulses in shallow waters (at 8 and 12 m) north of Cape Catoche (near 87.1°W–21.7°N) at periods ranging between 2 and 60 days. The upwelling pulses did not correlate with local wind-driven

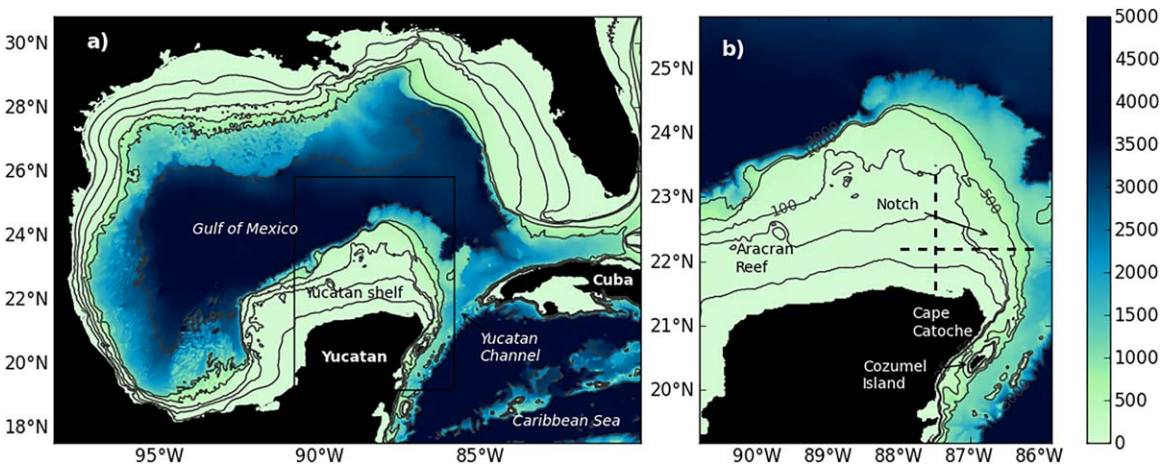

Figure 1. Map and bathymetry of the (a) Gulf of Mexico and (b) Yucatan shelf. Contours represent 25, 50, 100, 500, 1,000, and 3,000 m isobaths. The dashed lines in Figure 1b indicate the position of the sections shown in Figure 4.

Ekman transport, but they observed some correlation between northerly winds in the band 5–16 days and temperature increase suggesting that northerlies may be able to disrupt the upwelling at Cape Catoche.

If of topographic nature, the eastern Yucatan upwelling is expected to be influenced by changes in strength and position of the along shelf current. The Yucatan Current presents a strong variability caused by (1) anticyclonic and cyclonic eddies coming from the Cayman Basin (Athié et al., 2012; Cetina et al., 2006; Sheinbaum et al., 2016), (2) Loop Current (LC) extension (Bunge et al., 2002), (3) regional wind field (Chang & Oey, 2012), (4) topographic Rossby waves (Ezer et al., 2003), or (5) coastal trapped waves propagating from the western Gulf of Mexico (Jouanno et al., 2016). These different processes are expected to influence the Yucatan upwelling if there is a dynamic link between the Yucatan Current and the Yucatan upwelling. The mechanisms and temporal scales at play in the interaction between the along shelf current and the uplift of the deep waters to the shelf remain to be fully understood.

The aim of this study is to describe the variability of the Yucatan upwelling by using a set of high-resolution numerical simulations of the Gulf of Mexico and to shed light on the processes that contribute to this variability. The paper is organized as follows. Numerical experiments are presented in section 2. Section 3 describes the spatial and temporal characteristics of the Yucatan upwelling. The pathways of the upwelled

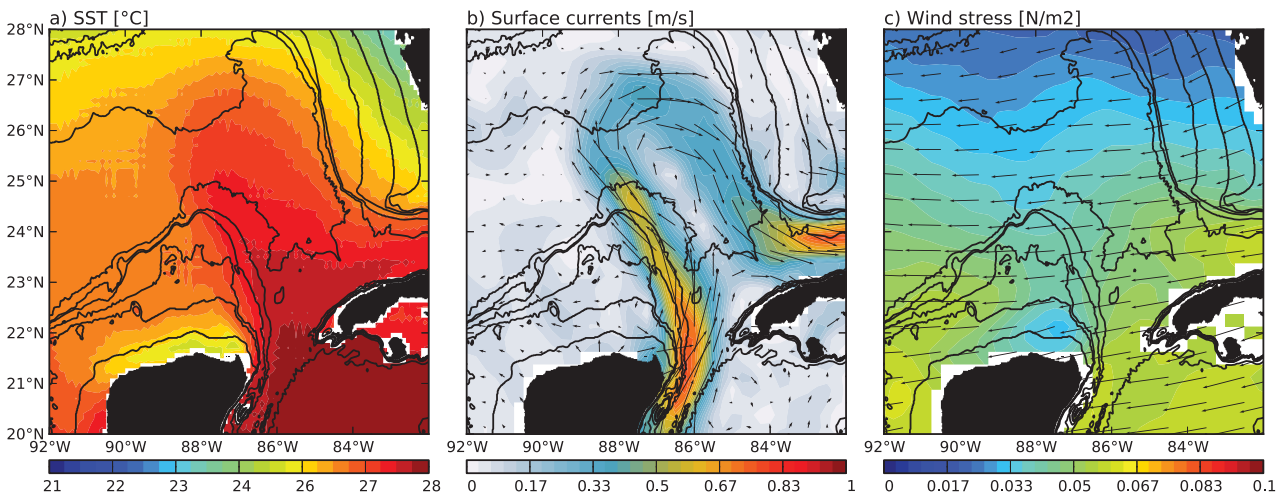

Figure 2. Climatological average of (a) observed sea surface temperature (°C), (b) surface currents (m s^{-1}; from altimetry and Ekman drift, GECKO product; Sudre et al., 2013), and (c) DFS5.2 wind stress (N m^{-2}) for the period 2008–2012. Contours show isobaths 25, 50, 100, 500, 1,000, and 3,000 m. SSTs observations are from the NOAA CoastWatch blended product (1/10° resolution).

waters are investigated from a Lagrangian perspective and sensitivity experiments are analyzed in order to identify the role of the notch on the east Yucatan shelf-slope. Finally, section 4 provides a discussion and summary of the results.

2. Numerical Simulations of the Gulf of Mexico

The regional model configuration used in this study has already been described and analyzed in Jouanno et al. (2016) which focused on the formation of Loop Current Frontal Eddies (LCFEs) in the Campeche Bank area. The numerical code is the oceanic component of the Nucleus for European Modeling of the Ocean program (NEMO3.6, Madec, 2016). It solves the three-dimensional primitive equations in spherical coordinates discretized on a C-grid and fixed vertical levels (z coordinate). The model configuration consists of a 1/36° grid ($\Delta x = \Delta y \approx 2.8$ km) of the Gulf of Mexico and Cayman Sea (98°W–78°W and 14°N–31°N). There are 75 levels in the vertical (with 12 levels in the upper 20 m and 24 levels in the upper 100 m). The vertical diffusion coefficients are given by a Generic Length Scale (GLS) scheme with a k-ε turbulent closure (Reffray et al., 2015). Bottom friction is quadratic with a bottom drag coefficient of 10^{-3} and partial slip boundary conditions are applied at the lateral boundaries.

The model is forced at its open boundaries with daily outputs from the MERCATOR global reanalysis GLORYS2V3. At the surface, the atmospheric fluxes of momentum, heat, and freshwater are computed by bulk formulae (Large & Yeager, 2009) and the DFS5.2 forcing set (Dussin et al., 2016) which consists of 3 h fields of wind, air temperature and humidity, and daily fields of long, short wave radiation, and precipitation. The regional model was initialized at day 1 January 2000 with temperature and salinity fields from GLORYS2V3 and has been integrated from 2000 to 2012. Daily averages from 2008 to 2012 are used in this study, so the upper ocean model solution has had time to stabilize.

We refer the reader to Jouanno et al. (2016) for further details on the numerical choices and some elements of validation of the reference simulation, including assessment of the regional surface currents and eddy kinetic energy and comparisons with in situ observations of currents in the 0–1,000 m depth range along the Yucatan shelf break.

In addition to the reference simulation (REF), two additional simulations have been performed: MONTHLY and NOTCH. In simulation MONTHLY, the surface wind stress is computed using monthly averages of the DFS5.2 10 m winds used in REF. In an attempt to investigate the role of the mechanical forcing produced by the high-frequency winds, the air-sea heat and freshwater fluxes (specifically the latent and sensible heat fluxes and the evaporation) in MONTHLY are computed using the high-frequency DFS5.2 winds used in REF as well. This strategy is motivated by two reasons. First, it allows to specifically isolate the mechanical impact of the wind, keeping the air-sea fluxes very close to the reference solution. Second, the averaged latent and sensible heat fluxes are largely influenced by the high-frequency fluctuations of the wind, so the use of filtered winds in the computation of the air-sea heat fluxes would lead to unrealistic SST and MLD, making the interpretation of the related sensitivity experiment difficult. In the NOTCH simulation, the topography of the eastern Yucatan shelf break is modified in order to remove the notch on the eastern Yucatan shelf break (the modification of the topography can be seen in Figures 3g–3i).

3. Characteristics of the Yucatan Upwelling

3.1. Temperature Variability Over the Shelf

The mean distribution of model SST (Figure 3a) reproduces the weak minimum of SST that is observed on the Yucatan shelf close to the shore (Figure 2a). It compares well with the satellite observations, including the presence of a band of warm SST along the Yucatan coast. An extensive field campaign along the Yucatan coast in summer 2006 revealed the presence of warmer waters in a thin band along the northern shore of the Yucatan peninsula (Enriquez et al., 2013) that closely resembles the band of warm temperature simulated by the model near the coast and inferred from satellite data (Figure 2a).

At 40 m, mean temperature distribution in the model reveals intrusion of cool waters from the eastern shelf break, near the notch, that spread over the shelf (Figure 3b). The mean tongue of cool waters at 40 m resembles the patterns of bottom temperature observed during different seasons in Merino (1997; see his Figures 3a and 3b): the tongue of cool waters extending (and narrowing) westward is centered between

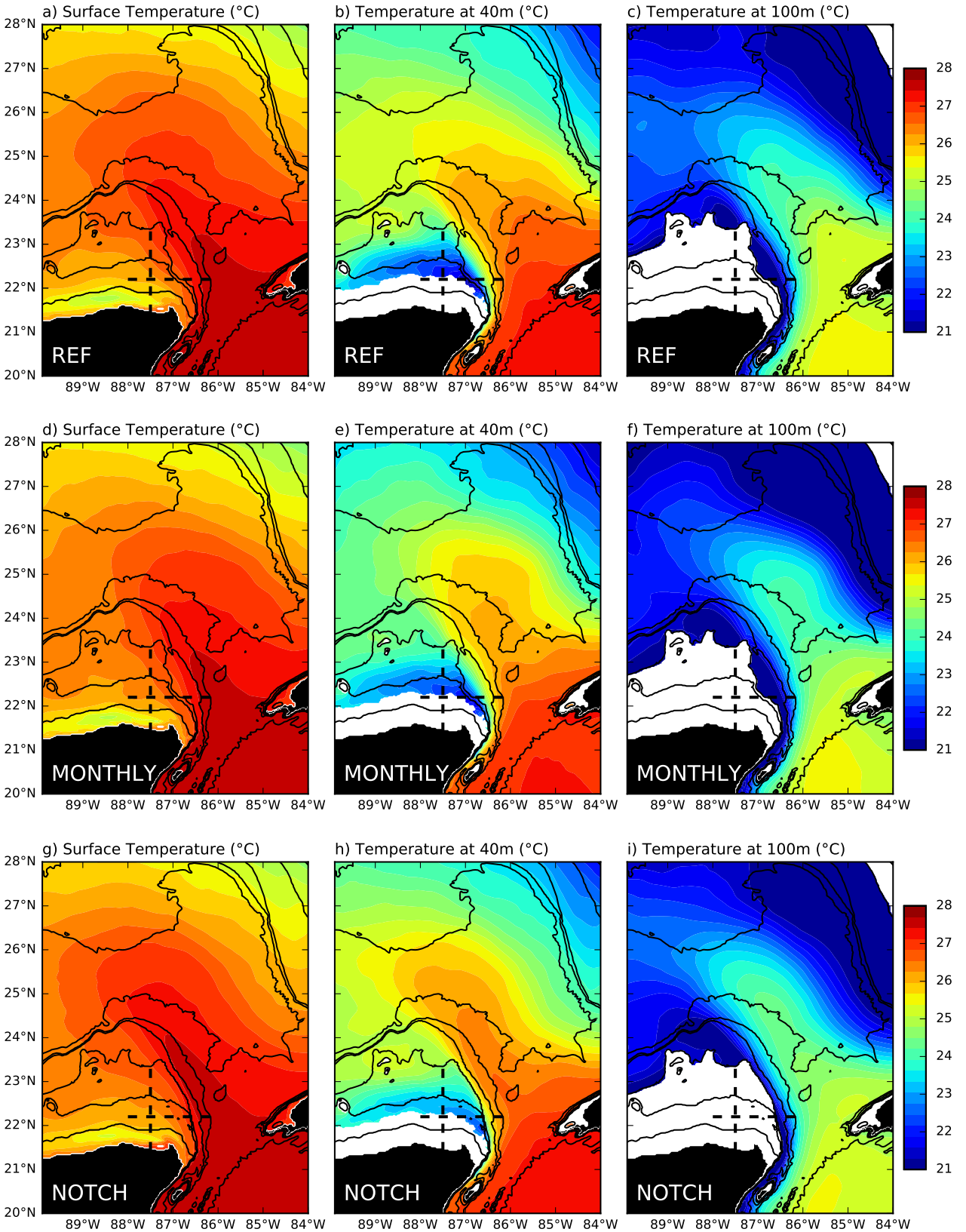

Figure 3. Climatological model temperature (°C) at the surface, 40 and 100 m for (a–c) REF, (d–f) MONTHLY, and (g–i) NOTCH simulations. The period used to compute the temporal mean is 2008–2012. The isobaths 25, 50, 100, 500, 1,000, and 3,000 m are shown with contours. The dashed lines indicate the position of the sections shown in Figure 4.

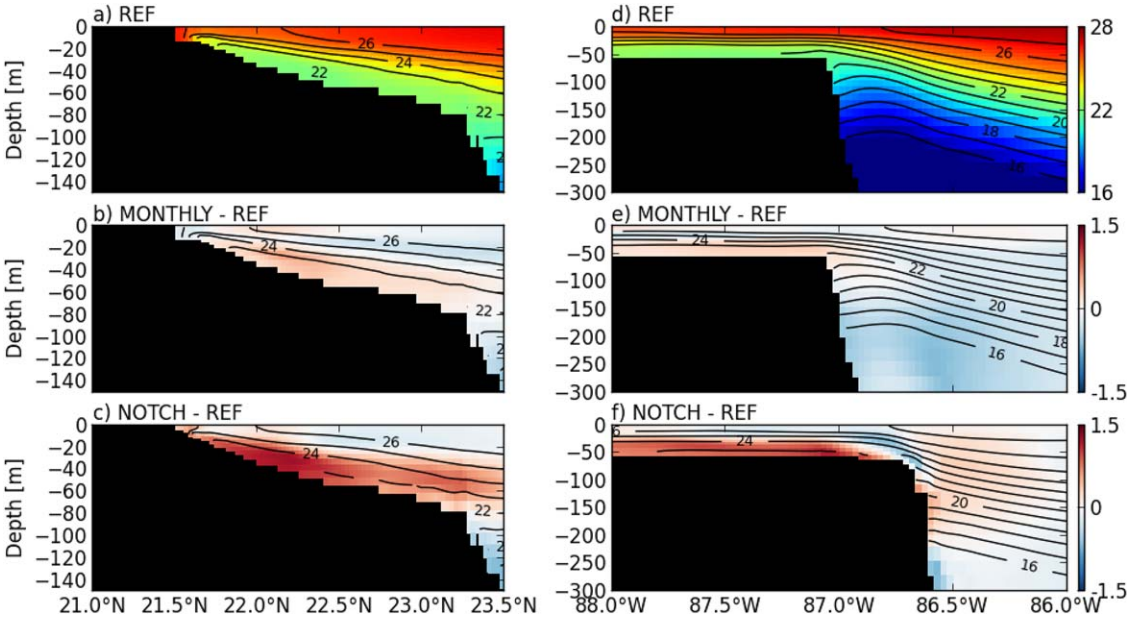

Figure 4. (a) Meridional section at 87.5°W and (d) zonal section at 22.2°N of time-averaged temperature (°C) for simulation REF over the period 2008–2012. Difference of temperature (in °C) between NOTCH and REF are shown in (b) and (e) and difference between MONTHLY and REF are shown in (c) and (f). A positive anomaly means that MONTHLY or NOTCH are warmer than REF. The contours represent the mean isotherms (from 16 and 28°C with 1°C interval) for each experiment. The positions of the sections are indicated in Figures 1b and 3.

the 40 and 50 m isobath, with the coolest temperatures observed at the east, near the southernmost part of the notch. Meridional and zonal sections (Figures 4a and 4d) of mean temperature also illustrate that the main signature of the upwelling is observed at subsurface, below 30 m depth. This is in agreement with in situ measurements by Merino (1997) and Enriquez et al. (2013).

The time evolution of the SST at 22.2°N–87.5°W shows strong seasonal variations in agreement with satellite observations (Figure 5a). The seasonal cycle of temperature is evident in the upper 20 m, with the warmest waters occurring between May and October (Figure 5b). To first order, the seasonal evolution of the SST (Figure 5a) is driven by air-sea fluxes (Figure 5d). During winter, intense wind bursts (Figure 5c) and associated surface heat loss (Figure 5d) are sometimes associated with a homogenization of the water column (Figure 5b), suggestive of intense mixing over the Yucatan shelf.

In the subsurface (below 20 m), the seasonal cycle is less clear and is not in phase with the evolution of the surface and near-surface temperatures (Figure 5b). Merino (1997) observed cool water over the shelf mostly during spring and summer, suggesting that the seasonal cycle of the upwelling is asymmetrical in time, with an abrupt intrusion of cool water during spring and a spin down of this process during the rest of the year. Unlike the observations, the numerical simulation suggests that cool conditions on the eastern Yucatan shelf can also occur during winter (years 2009 and 2011 in Figure 5b) or can be reinforced during summer (years 2008 and 2012).

3.2. Pathways and Origin of the Cool Water Parcels

The mechanisms that bring water to the Yucatan shelf are now investigated from a Lagrangian perspective. Parcels are launched on the Yucatan shelf and traced backward in time during 60 days using the Lagrangian tool ARIANE (Blanke & Raynaud, 1997). Inferred trajectories are not influenced by subgrid mixing and surface heat fluxes, making this diagnostic well suited to the study of upwelling processes. Water parcels (∼180,000 in total) are seeded every 2 days from January 2008 to December 2012, approximately every 10 km, between 89°W and 87°W and between the coast and 22.6°N (see black box in Figure 6a), at 30, 40, and 50 m depth. The binned (averaged) distribution of the water parcels integrated backward 10, 30, and 50 days from their initial position is shown in Figures 6a–6c. It suggests that the largest part of the upwelled waters over the shelf are advected from the Yucatan Current through the notch of the eastern Yucatan shelf.

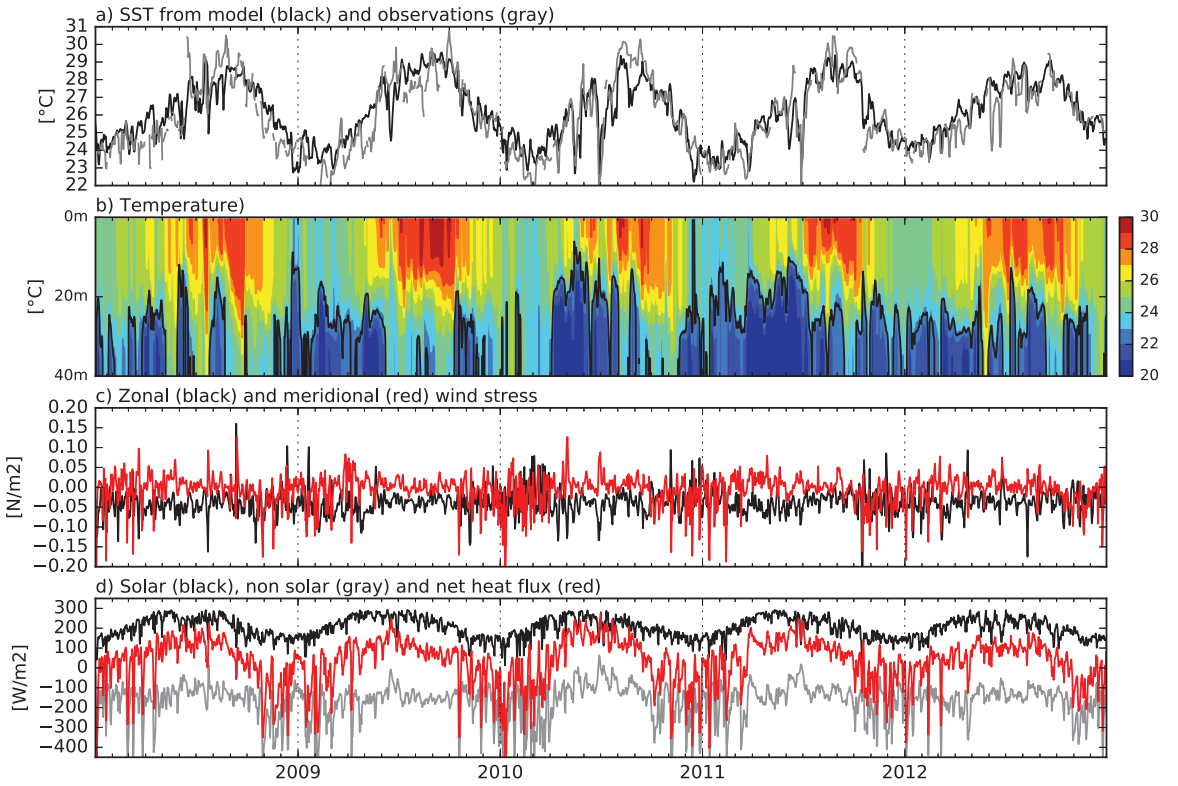

Figure 5. Time series at 87.5°W–22.2°N over the Campeche Bank: (a) SST (°C) from model (black) and satellite (gray), (b) temperature profile (°C), (c) zonal (black) and meridional (red) wind stress (N m^{-2}), and (d) net air-sea heat flux (red) together with the solar (black) and nonsolar components (gray; W m^{-2}).

The binned position (0.1° × 0.1°) of the water parcels the last time they crossed the 50, 100, and 150 m depth before reaching the Yucatan shelf (i.e., the black box in Figure 6a) is shown in Figure 7. About 96% of the subsurface water parcels that reach the Yucatan shelf (in less than 30 days) are advected from below 50 m (Figure 7a), 66% from below 100 m (Figure 7b), and 24% from below 150 m (Figure 7c). This confirms that a large fraction of the waters located below 30 m on the Yucatan shelf have been upwelled. Moreover, the location where the parcels cross the different depths suggests that the notch of the Campeche Bank is a key geographical feature for this particular upwelling system (Figures 7a–7c). Although weak, a secondary upwelling location is identified east of Cape Catoche (21°N–86.5°W), where isobaths diverge (Figure 7a).

A quantitative analysis is carried out in order to estimate the transport of cool water reaching the Yucatan peninsula that originates in the Caribbean Sea. This can be quantified using the Lagrangian analysis in a quantitative way (see for instance Blanke & Raynaud, 1997), taking advantage of the Lagrangian trajectory scheme that respects mass conservation. A fixed elementary transport is associated with each particle so that a Lagrangian transport can be computed between an initial seeding section on the Yucatan shelf (S0; referred to as the "arrival section") and backward arrival sections (S1 and S2; referred to as the "source sections"). These sections are shown in Figure 8a. The water parcels are seeded every day at S0 from 2009 to 2012 and are advected backward until reaching S1 or S2 with a time threshold of 365 days.

The binned distribution of Lagrangian transport as a function of temperature is shown at sections S0, S1, and S2 in Figures 8b–8d, for water parcels initialized at S0 and intercepted (backward) at sections S1 and S2 (Figure 8a). The binned distribution at section S0 for REF confirms that waters with temperatures between 17 and 29°C are transported over the Yucatan shelf (Figure 8b). The largest part of the transport (>10 × 10^4 m^3 s^{-1}) occurs for water parcels with temperatures between 21 and 28°C, consistent with the mean temperature found on the Yucatan shelf west to 87°W (Figure 4d). At the source section S1, the binned distribution of transport is skewed toward cooler temperatures with transport of water parcels with temperature reaching down to 15°C. The difference of distribution between S0 and S1 indicates that during their route to the shelf, the upwelled water parcels suffer temperature changes which are expected due to both vertical

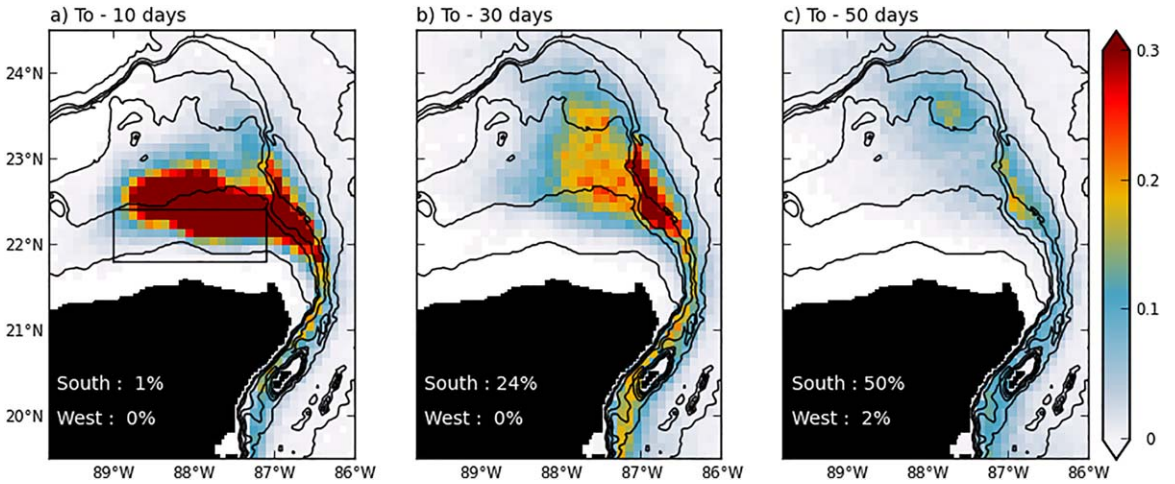

Figure 6. Distribution of water parcels before their arrival on the Yucatan shelf. The parcels of water are released every 2 days from 2008 to 2012 in the subdomain indicated by the black box in (a), every 10 km at 30, 40, and 50 m depth. They are integrated backward for 50 days. The number of water parcels is then counted by bins of 0.1° × 0.1° and is shown at lags between (a) −10 days, (b) −30 days, and (c) −50 days as a percentage of the total number of water parcels. A total of ∼180,000 water parcels were released. The percentages of parcels reaching the southern and western boundaries of the figure domain are also indicated.

mixing and air-sea fluxes in the upper layers. Some Yucatan shelf waters are also advected from section S2 (Figure 8d), but their contribution to the transport on the Campeche Bank is much weaker (up to 1 order of magnitude) than waters coming from section S1.

In order to verify the importance of the notch in the upwelling process, the simulation NOTCH with modified bathymetry at the Yucatan shelf break (see Figure 3g) is compared with simulation REF. The mean temperature at the bottom of the Yucatan shelf is about 1.5°C lower in REF than in NOTCH (Figures 3g–3i, 4c, and 4f). The larger temperature anomalies are confined to the bottom layer of the Yucatan shelf, between 30 and 60 m, while the temperature in the upper 20 m is almost not affected by the presence of the notch (Figures 4c and 4f).

The quantitative Lagrangian analysis further indicates that when the notch is removed the following changes occur: (i) the amount of cool water entering the Yucatan shelf at section S0 is decreased by 55% compared to REF (the overall transport of waters over the Yucatan shelf is reduced from 0.225 to 0.101 Sv) and (ii) their source temperature is warmer (Figure 8c).

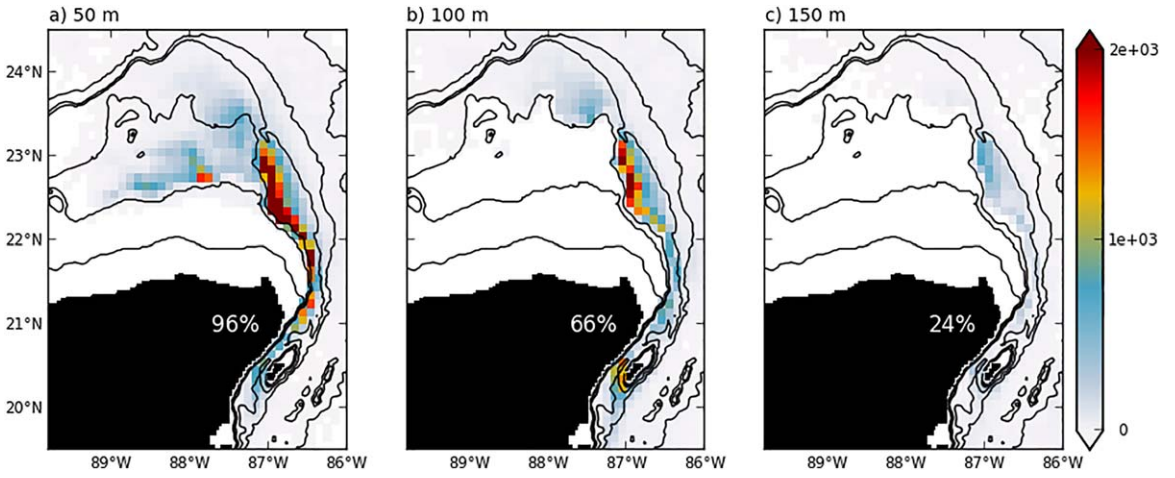

Figure 7. Binned distribution of the water parcels the last time they cross the (a) 50, (b) 100, and (c) 150 m isobath before reaching the subdomain shown in Figure 6a over the Yucatan shelf. The percentages of water parcels originating bellow 50, 100, and 150 m depth are 96, 66, and 24% respectively (for a total of 183,000 water parcels released).

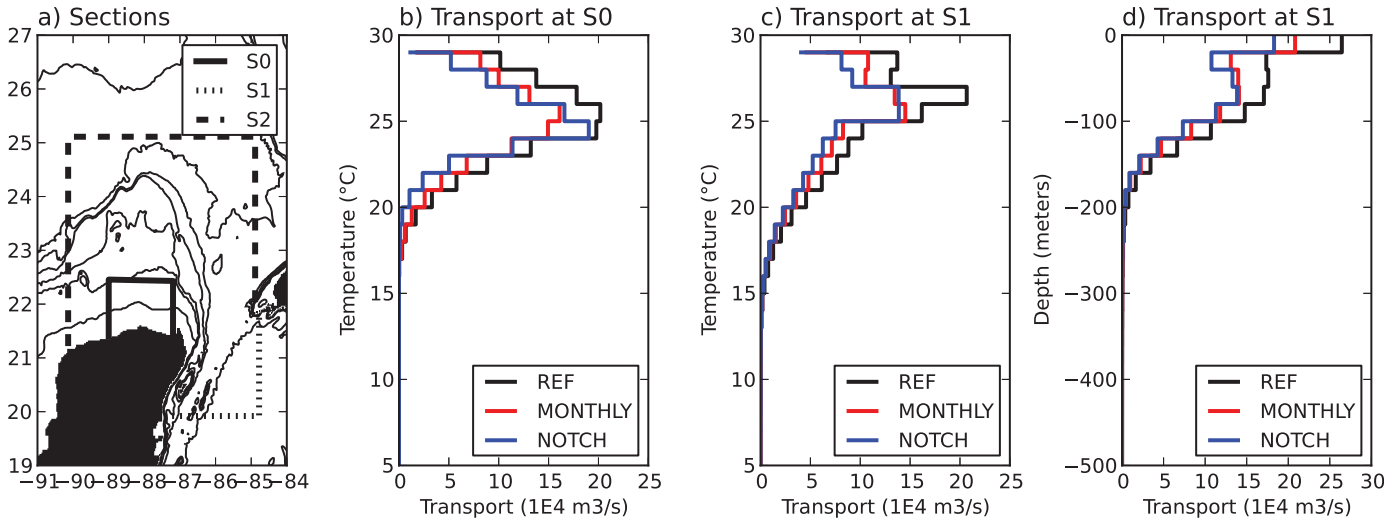

Figure 8. Quantitative Lagrangian analysis: (a) location of the water parcels seeding section S0 and interception sections S1 and S2, (b–d) binned transport ($m^3\ s^{-1}$) at section S0, S1, and S2 as a function of temperature. Particles have been seeded at section S0 each day from 1 January 2009 to 31 December 2012 and integrated backward until reaching the interception sections S1 and S2, with an integration time limit of 365 days.

3.3. Variability of the Upwelling Process

The time series of transport of cool waters (<22.5°C) on the Yucatan shelf through section S0 is shown in Figure 9a suggesting a marked low-frequency variability (as indicated by the 30 day low-pass filtered time series; red line) with maxima that tend to occur during spring (with the exception of year 2012). For REF, the transport spectra show two main peaks of variability: the nearly annual low-frequency mode observed in Figure 9a and a high-frequency mode at periods below 15 days with maximum variance in the 6–8 days band (Figure 9d).

3.3.1. Low-Frequency Mode

The relationship between Yucatan shelf temperatures and LC dynamics is further analyzed by time averaging model fields during periods with large and weak transport of cool waters (<22.5°C) through S0 (Figure 9a). A 30 days running mean has been applied to the transport time series through S0 in order to

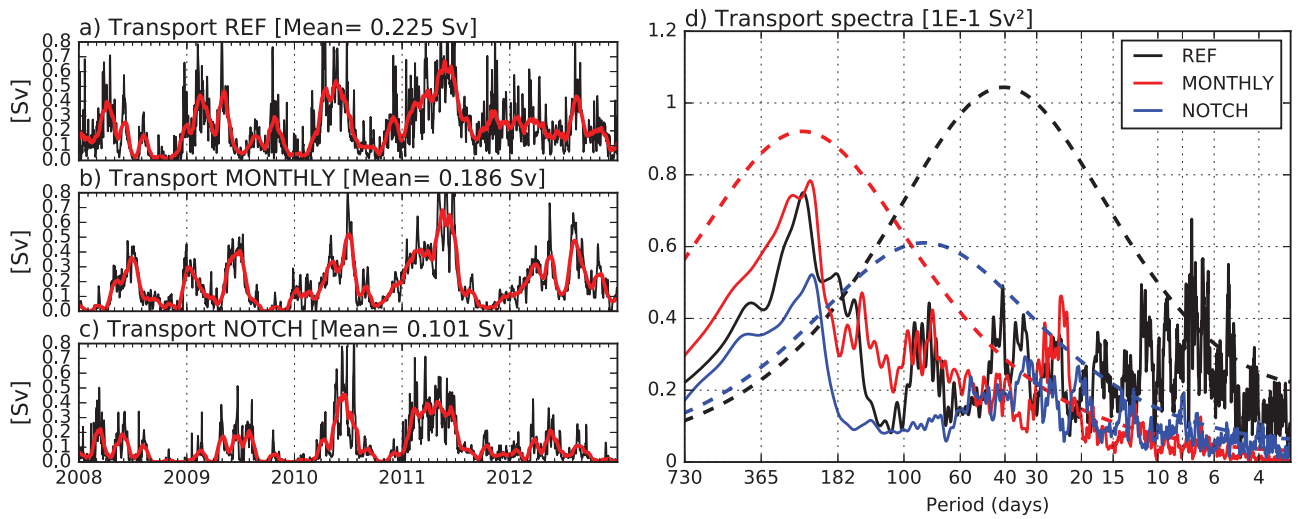

Figure 9. Series of transport (units are Sv, $10^{-6}\ m^3\ s^{-1}$) entering section S0 (see Figure 8a) only for water parcels with temperature <22.5°C for simulations (a) REF, (b) MONTHLY, and (c) NOTCH. The 30 days running mean low-pass filtered time series are superimposed in red. (d) Multitaper variance-conserving power spectra (Sv^2) of the transport time series (Thomson, 1982). The multitaper spectra are built with five tapers. Dotted lines represent the corresponding 90% confidence limit based on the theoretical spectra of an AR(2) process with variances equal to that of the analyzed signals. The number of degrees of freedom for the 90% level calculation is estimated as 2K-1, with K the number of windows.

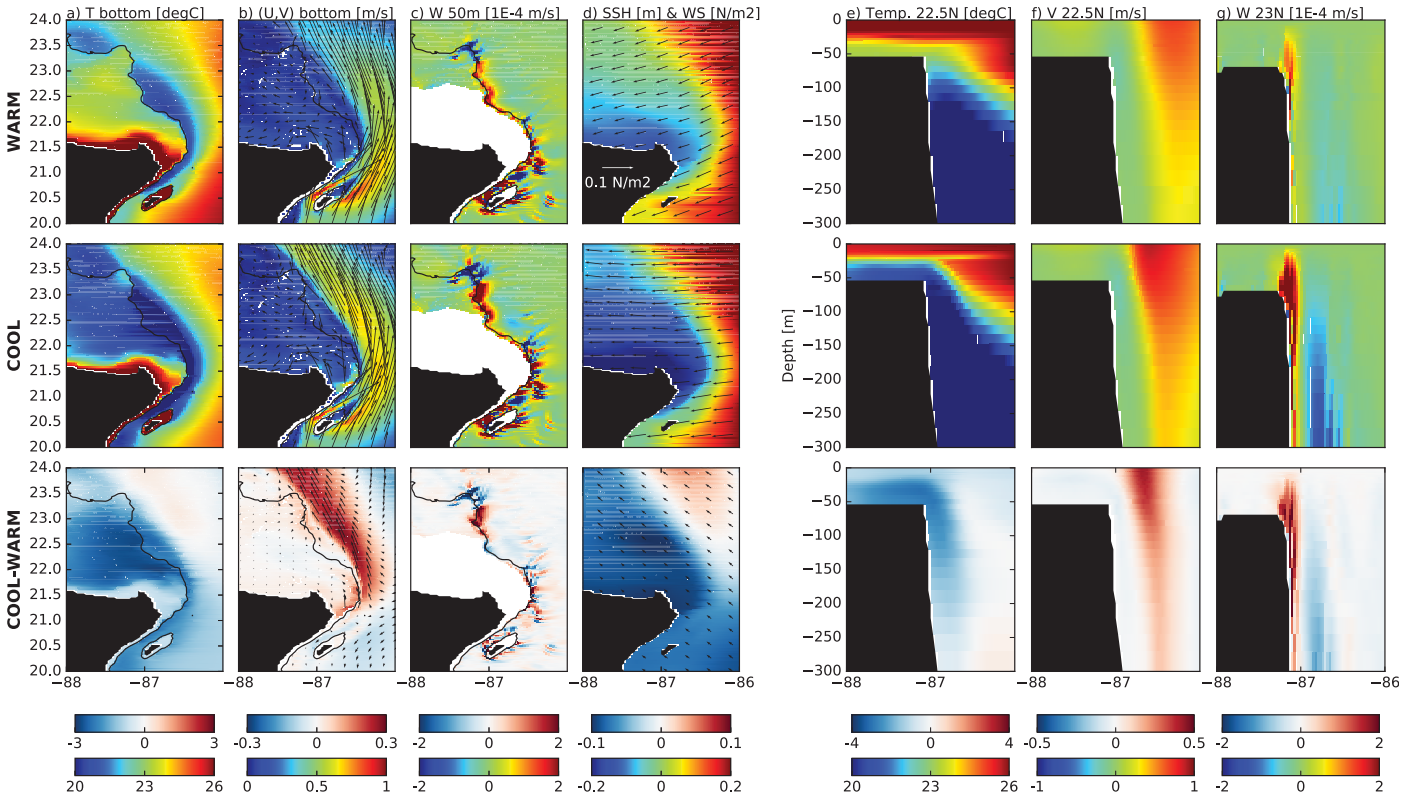

Figure 10. Comparison between periods with (top row) warm and (middle row) cool conditions of temperature at the Campeche Bank. Warm and cool conditions are identified by selecting 33% of the days of the 5 years model run with the weakest and largest transport of waters with temperature below 22.5°C through section S0 (see Figure 9a). The high-frequency variability of the transport time series has been removed using a 1 month running mean before identifying the cool and warm periods (red curve in Figure 9a). Composite model fields are built for (a) temperature at 100 m (units: °C), (b) currents at 100 m (units: m s^{-1}), (c) vertical velocity at 50 m (units: m s^{-1}), (d) sea level and wind-stress vectors (units: m and N m^{-2}), (e) temperature at 22.5°N (units: °C), (f) meridional velocity at 22.5°N (units: m s^{-1}), and (g) vertical velocity at 23°N (units: m s^{-1}). Difference between both periods are shown in the bottom row. In Figures 10a and 10b, bottom temperatures and currents are shown where the ocean floor is above 100 m.

smooth-out the high-frequency fluctuations of the transport. The periods with large and weak transport were selected as the dates with smoothed transport ranging within the upper and lower third of the smoothed transport values (this corresponds to threshold values of 26×10^4 and 15×10^4 m^3 s^{-1} respectively). Composites representative of the periods with large and weak transport are shown in Figure 10. During periods with increased transport of cool water through S0, the bottom temperature on the Yucatan shelf is 3–4°C cooler compared to periods with weak transport (Figure 10a), and the western edge of the Loop Current shows larger surface velocities (Figure 10b).

Two mechanisms are hypothesized to contribute to the link between intensified Loop Current and cooler conditions on the Yucatan shelf. First, the zonal tilting of the isotherms along the Yucatan shelf break, which is closely linked to the strength of the Loop Current through thermal wind balance, brings cool waters closer to the Yucatan shelf. Compared to warm conditions, the Loop Current speed at 100 m depth during cool conditions is 0.3 m s^{-1} larger (Figure 10b) and waters along the shelf and within the notch are 2°C cooler (Figures 10a and 10e). Second, the position and strength of the Loop Current drive vertical velocities along the Yucatan shelf break and thus the amount of water brought to the Yucatan shelf: the vertical velocities at 50 m at the northern part of the notch (~23°N) are ~2 times larger (Figures 10c and 10g) when the Loop Current is intensified at the Yucatan shelf break (Figure 10b and 10f).

The enhancement of the vertical velocity along the northern part of the notch may be an important component of the upwelling response due to advection-driven LC flow over a submarine canyon (see for instance Allen & Hickey, 2010): the LC fluid column is stretched to conserve potential vorticity (PV), generating elliptical cyclonic eddies with an upwelling cell of vertical velocity located at the northern vertex of the notch-constrained PV ellipse (Viúdez & Dritschel, 2003).

3.3.2. High-Frequency Mode

A linear regression analysis is performed in order to further understand the structure and forcing of the high-frequency pulses of transport of cool water over the Yucatan shelf (Figure 9). Model key variables are regressed on a high-frequency transport index, which is defined as the transport of cool waters (<22.5°C) through section S0, computed each day from 2008 to 2012 and high-pass filtered using a Lanczos filter with a cutoff period of 15 days. Regression coefficients between the index and the model fields are computed at each model grid point and are shown in Figure 11. The transport index has been normalized by its standard deviation, so the regression coefficient may be interpreted as the anomalous pattern linearly correlated with a one standard-deviation anomaly of high-frequency cool water transport through S0 (about 9×10^4 $m^3\ s^{-1}$) and is therefore expressed in the units of the regressed variable. In order to help the discussion, we show on the last column of Figure 11 the mean distribution of the different fields that have been regressed.

The lagged regressions of the model key variables are shown from lag −2 (in days) to lag +3 days in Figure 11. The time evolution of the regressed 100 m depth temperature anomalies (and bottom temperature anomalies when the topography is shallower than 100 m) shows a negative anomaly originated near the notch at lag −1 day, growing and propagating to the west from lag 0 to lag +2 (Figures 11a and 11e). At lag +3 days, the correlation weakens, and the anomaly will move back eastward at subsequent lags (not shown). By construction, the maximum input of cool water over the shelf occurs at lag 0 (with strong westward current anomalies over the Yucatan shelf transporting cool waters). This maximum of transport occurs while a coastal wave is traveling on the Yucatan shelf and interacts with the LC (Figure 11b). The bottom temperature anomaly originates on the southern part of the notch (Figure 11a), in agreement with the

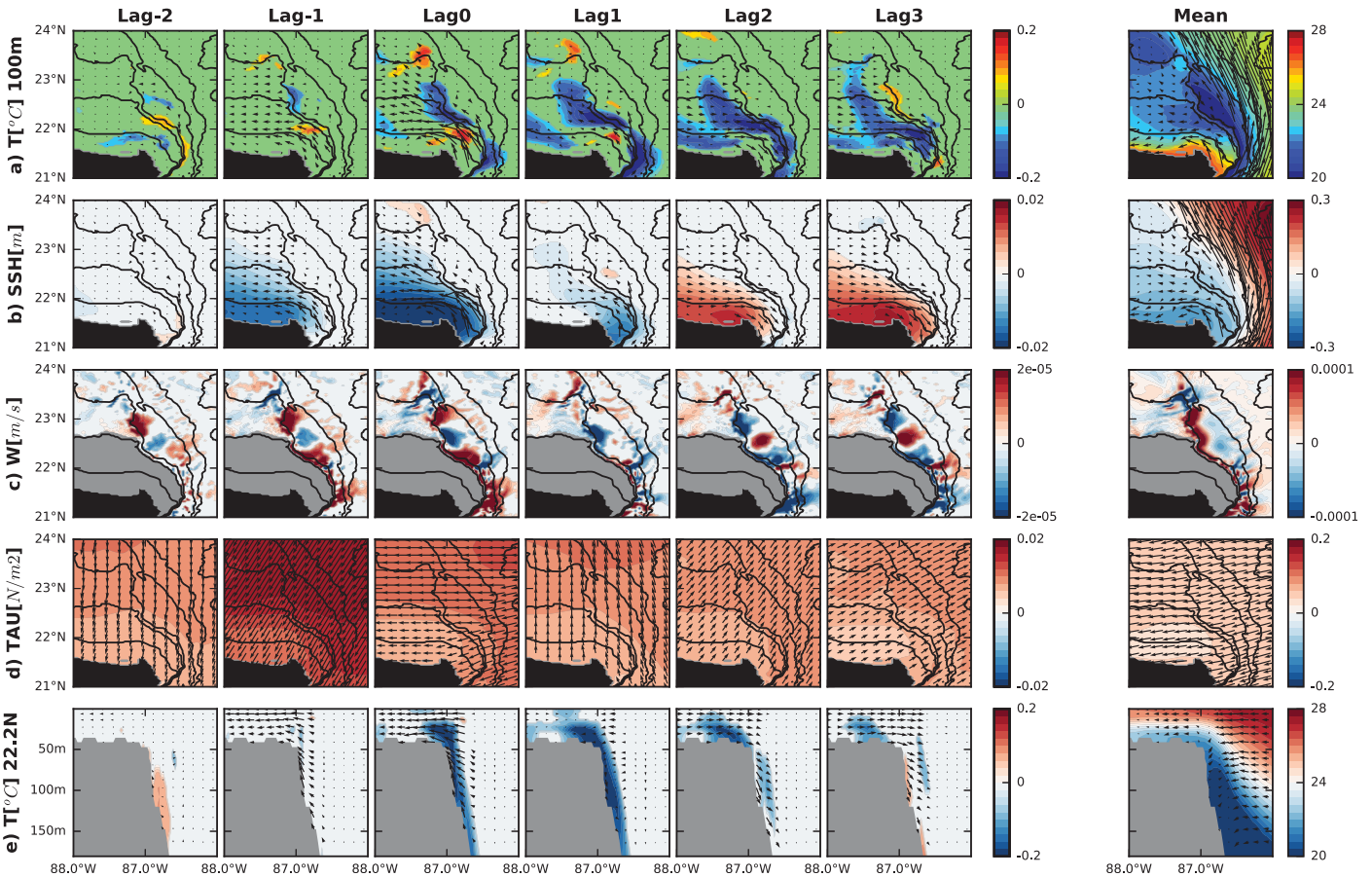

Figure 11. Linear lagged regressions of different model outputs on an index of high-frequency transport of cool waters. Lags range from −2 days to + 3 days. To compute this index, the daily transport through section S0 of waters cooler than 22.5°C has been low-pass filtered with a Lanczos filter to retain the variability below 15 days. Regression coefficients are shown for maps of (a) temperature (°C) and currents at 100 m depth (and at the bottom where the ocean is shallower than 100 m), (b) sea level height (m), (c) vertical velocity at 50 m (m s^{-1}), (d) wind stress (N m^{-2}), and (e) a zonal section of temperature and currents (u,w) at 22.2°N. Correlation coefficients below the 90% confidence level are set to 0.

qualitative Lagrangian analysis (Figure 7a). The vertical velocity anomalies at 50 m show an alternation of positive and negative anomalies along the Yucatan shelf traveling slowly to the north (Figure 11c). Upward anomalies at the southern part of the notch (22.2°N) peak at lag 0 and are expected to directly contribute to the advection of the cool waters over the Yucatan shelf. The coastal depression of the sea surface height (Figure 11b) is forced by a southward wind burst at lag −1 (Figure 11d). We also note a weaker correlation with southward winds at lag −8 day (not shown), which is in agreement with the forcing of coastal trapped waves in the northeastern Gulf of Mexico by the cold front passages during autumn and winter. These waves travel anticlockwise around the gulf and have a significant signature on the Yucatan shelf (see Jouanno et al., 2016). Although it is difficult to differentiate their effect from the direct response of the surface currents to winds over the Yucatan shelf at lag −1 day, the regression analysis suggests that they only have a second order influence on the Yucatan upwelling pulses.

The results above suggest an apparent positive correlation between the intensity of the upwelling response and the cold front passages and raise the question of whether this high-frequency coastal waves (either locally or remotely forced) have a net impact on the Yucatan upwelling (i.e., do they increase the overall amount of subsurface cool water that is brought to the Campeche platform)? Part of the answer is provided by the analysis of simulation MONTHLY for which submonthly wind-stress forcing has been removed. We verify that when forcing the model with monthly wind stress, the high-frequency variability of the transport is strongly reduced (Figures 9b and 9d), further confirming that the high-frequency pulses of transport are forced to first order by the high-frequency fluctuations of the winds. Most interesting, the 5 year averaged transport of cool waters through S0 is decreased by 17% compared to REF (from 0.225 to 0.186 Sv), indicating that high-frequency winds participate in the net upwelling. This is in agreement with the Yucatan shelf subsurface temperature which is warmer (∼+0.3°C) in MONTHLY compared to REF (Figures 3d–3f, and 4b, and 4e).

Interestingly, we note that when the notch is removed, the high-frequency mode of transport of cool waters is notably reduced (Figures 9c and 9d), indicating that the notch also impacts the high-frequency variability of the Yucatan upwelling response.

4. Conclusions

This study describes the variability of the eastern Yucatan upwelling using a set of high-resolution (1/36°) numerical simulations of the Gulf of Mexico and sheds light on the dynamical processes that drive this variability. Results suggest that the Yucatan upwelling is a complicated dynamical system involving several mechanisms and modes of variability. The main findings of this study are as follows:

1. A Lagrangian quantitative analysis of the model results does show that the largest fraction of the upwelled waters is advected from the Yucatan Channel through the notch of the eastern Yucatan shelf break, in agreement with the hypothesis formulated in Merino (1997).
2. The interaction of the Loop Current with the topography (i.e., the notch) enhances the upwelling through development of intense vertical velocities, O(w) = 10^{-4} m s^{-1}, along the Yucatan shelf.
3. There are two distinct modes of variability of the Yucatan upwelling. A low-frequency mode driven by the low-frequency fluctuations of the Loop Current strength and a high-frequency mode forced by high-frequency wind fluctuations over the Yucatan shelf. This makes it difficult to clearly define the duration of an upwelling event.
4. High-frequency winds make a net contribution to the upwelling. This point out that high-frequency winds need to be considered to properly asses all mechanisms involved in the upwelling process.

We showed that the low-frequency variability of the upwelling is connected with the Yucatan and Loop Current strength and position. From Figures 9a–9c, a seasonal cycle of the upwelling seems to show up in the different simulations, with maximum upwelling that would occur in spring-summer. This is consistent with the seasonality of the upwelling as observed by Merino (1997). Nevertheless, the large variability (from intraseasonal to interannual time scales) of the Yucatan upwelling shown in our 5 years simulations call for caution. More model and observational data are required to confirm whether the seasonal cycle of the upwelling that seems to emerge from our set of simulations can be considered as a robust feature of the system.

Although the topographic nature of the Yucatan upwelling has been confirmed by this investigation, the mechanisms at play along the Yucatan shelf break still remain to be fully clarified. There are different processes by where the current-topography interaction could contribute to upwell the waters over the Yucatan shelf: Ekman response to bottom friction (Roughan & Middleton 2004), or more broadly canyon related dynamics (Allen & Durrieu de Madron, 2009; Kämpf, 2012). Clarifying the mechanisms controlling the vertical velocity on the Yucatan shelf will be the subject of a future study.

Acknowledgments

This research has been supported by IRD and is a contribution of the Gulf of Mexico Research Consortium (CIGoM), funded by the National Council of Science and Technology of Mexico—Secretariat of Energy -Hidrocarbons Trust, project 201441. Supercomputing facilities were provided by GENCI project GEN7298 and CICESE. We acknowledge C. Rousset, S. Masson, G. Madec, and R. Benshila from the NEMO team for their help in setting up the configuration. Model results can be reproduced by using the ocean code NEMO3.6_stable-rev4791 (http://forge.ipsl.jussieu.fr/nemo/wiki/Users). We acknowledge B. Blanke and N. Grima for making the ARIANE code available (http://stockage.univ-brest.fr/~grima/Ariane/), and the MEOM team in Grenoble for providing the DFS5.2 forcing set (http://servdap.legi.grenoble-inp.fr/meom/DFS5.2/). GECKO data are available at http://ctoh.legos.obs-mip.fr/products/global-surface-currents/global-surface-current-data-product. Finally, we are grateful to Martín Merino-Ibarra and another anonymous reviewer for their useful comments on the manuscript.

References

Allen, S. E., & Durrieu de Madron, X. (2009). A review of the role of submarine canyons in deep-ocean exchange with the shelf. *Ocean Science*, *5*(4), 607–620.

Allen, S. E., & Hickey, B. M. (2010). Dynamics of advection-driven upwelling over a shelf break submarine canyon. *Journal of Geophysical Research: Oceans*, *115*, C08018. https://doi.org/10.1029/2009JC005731

Athié, G., Candela, J., Ochoa, J., & Sheinbaum, J. (2012). Impact of Caribbean cyclones on the detachment of Loop Current anticyclones. *Journal of Geophysical Research: Oceans*, *117*, C03018. https://doi.org/10.1029/2011JC007090

Belousov, I. M., Ivanov, Y. A., Pasternak, S. A., Rass, T. S., & Rossov, V. V. (1966). Oceanographic research by the Soviet-Cuban Marine Expedition. *Oceanology*, *6*, 312–320.

Blanke, B., & Raynaud, S. (1997). Kinematics of the Pacific Equatorial Undercurrent: An Eulerian and Lagrangian approach from GCM results. *Journal of Physical Oceanography*, *27*, 1038–1053. https://doi.org/10.1175/1520-0485(1997)027

Bunge, L., Ochoa, J., Badan, A., Candela, J., & Sheinbaum, J. (2002). Deep flows in the Yucatan Channel and their relation to changes in the Loop Current extension. *Journal of Geophysical Research: Oceans*, *107*(C12), 3233. https://doi.org/10.1029/2001JC001256

Cetina, P., Candela, J., Sheinbaum, J., Ochoa, J., & Badan, A. (2006). Circulation along the Mexican Caribbean coast. *Journal of Geophysical Research: Oceans*, *111*, C08021. https://doi.org/10.1029/2005JC003056

Chang, Y. L., & Oey, L. Y. (2012). Why does the Loop Current tend to shed more eddies in summer and winter? *Geophysical Research Letters*, *39*, L05605. https://doi.org/10.1029/2011GL050773

Cochrane, J. D. (1966). *The Yucatan Current, upwelling off Northeastern Yucatan, and currents and waters of Western Equatorial Atlantic. Oceanography of the Gulf of Mexico* (Progress Rep., Ref. No. 66-23T, pp. 14–32). Houston, TX: TAMU.

Dussin, R., Barnier, B., & Brodeau, L. (2016). *The making of Drakkar forcing set DFS5* (DRAKKAR/MyOcean Rep. 01–04-16). Grenoble, France: LGGE.

Enriquez, C., & Mariño-Tapia, I. (2014). *Mechanisms driving a coastal dynamic upwelling*. Paper presented at Proceedings of the 17th Physics of Estuaries and Coastal Seas (PECS) Conference, Porto de Galinhas, Pernambuco, Brazil.

Enriquez, C., Mariño-Tapia, I., Jeronimo, G., & Capurro-Filograsso, L. (2013). Thermohaline processes in a tropical coastal zone. *Continental Shelf Research*, *69*, 101–109.

Ezer, T., Oey, L. Y., Lee, H. C., & Sturges, W. (2003). The variability of currents in the Yucatan Channel: Analysis of results from a numerical ocean model. *Journal of Geophysical Research*, *108*(C1), 3012. https://doi.org/10.1029/2002JC001509

Jouanno, J., Ochoa, J., Pallàs-Sanz, E., Sheinbaum, J., Andrade, F., Candela, J., et al. (2016). Loop Current Frontal Eddies: Formation along the Campeche Bank and impact of coastally trapped waves. *Journal of Physical Oceanography*, *46*(11), 3339–3363.

Kämpf, J. (2012). Lee effects of localized upwelling in a shelf-break canyon. *Continental Shelf Research*, *42*, 78–88.

Large, W. G., & Yeager, S. (2009). The global climatology of an interannually varying air-sea flux data set. *Climate Dynamics*, *33*, 341–364. https://doi.org/10.1007/s00382-008-0441-3

Madec, G., & the NEMO Team. (2016). *NEMO ocean engine* (Note du Pôle de modélisation de l'Institut Pierre-Simon Laplace Rep. 27). Paris, France: IPSL.

Merino, M. (1997). Upwelling on the Yucatan shelf: Hydrographic evidence. *Journal of Marine Systems*, *13*, 101–121.

Reffray, G., Bourdalle-Badie, R., & Calone, C. (2015). Modelling turbulent vertical mixing sensitivity using a 1-D version of NEMO. *Geoscientific Model Development*, *8*, 69–86. https://doi.org/10.5194/gmd-8-69-2015

Reyes-Mendoza, O., Mariño-Tapia, I., Herrera-Silveira, J., Ruiz-Martínez, G., Enriquez, C., & Largier, J. L. (2016). The effects of wind on upwelling off Cabo Catoche. *Journal of Coastal Research*, *32*(3), 638–650.

Roughan, M., & Middleton, J. H. (2004). On the East Australian Current: Variability, encroachment, and upwelling. *Journal of Geophysical Research: Oceans*, *109*, C07003. https://doi.org/10.1029/2003JC001833

Sheinbaum, J., Athié, G., Candela, J., Ochoa, J., & Romero-Arteaga, A. (2016). Structure and variability of the Yucatan and loop currents along the slope and shelf break of the Yucatan channel and Campeche bank. *Dynamics of Atmospheres and Oceans*, *76*, 217–239.

Sudre, J., Maes, C., & Garçon, V. (2013). On the global estimates of geostrophic and Ekman surface currents. *Limnology and Oceanography: Fluids and Environments*, *3*, 1–20. https://doi.org/10.1215/21573689-2071927

Thomson, D. J. (1982). Spectrum estimation and harmonic analysis. *Proceedings of the IEEE*, *70*(9), 1055–1096.

Viúdez, A., & Dritschel, D. (2003). Vertical velocity in mesoscale geophysical flows. *Journal of Fluid Mechanics*, *483*, 199–223.